Aerodynamic Performance Improvements Due to Porosity in Wings at Moderate Re

Yohanna G. T. Hanna* and Geoffrey R. Spedding†
University of Southern California, Los Angeles, CA 90089, USA

Small wings at moderate Re may have unpredictable performance characteristics, such as hysteresis loops in lift, due to the formation and movement of laminar separation bubbles. Even when the flow is seemingly simple, the outcomes may be counter-intuitive. As an example, the NACA 0012, a symmetric airfoil, at Re $= 5 \times 10^4$ has been shown to produce negative lift at small positive angles of attack. Natural flyers, such as birds and bats, occupy a similar Re regime, and it is natural to enquire how they deal with such sensitivities. Feathers are flexible and porous, and while flexibility has been much studied, the effect of porosity is less well-known. This study examines the effect of porosity on the performance of a NACA 0012 at Re$= 5 \times 10^4$ and demonstrates that even small permeabilities can significantly affect wing performance.

I. Nomenclature

AR	=	aspect ratio	Q	=	volume flow rate [m³/s]
b	=	span [m]	Re	=	chord based Reynolds number
c	=	chord [m]	Re_d	=	Reynolds number of pipe flow in pore
C_d	=	sectional drag coefficient	Re_x	=	Reynolds number as a function of x
C_ℓ	=	sectional lift coefficient	S	=	planform area [m²]
C_{ℓ_α}	=	lift curve slope	S_H	=	total hole planform area [m²]
C_p	=	pressure coefficient	t	=	airfoil thickness [m]
d	=	pore diameter [m]	U	=	freestrean velocity [m/s]
D	=	drag force [N]	$u_\perp$	=	pore disturbance [m/s]
D'	=	drag force per unit span [N/m]	x	=	streamwise direction [m]
f	=	friction factor	$\overline{x}_s$	=	top chord normal separation location
L	=	lift force [N]	y	=	spanwise direction [m]
L'	=	lift force per unit span [N/m]	z	=	cross-stream direction [m]
L/D	=	lift to drag ratio	α	=	angle of attack [°]
l_i	=	pore length [m]	δ	=	boundary layer thickness [m]
m	=	number of holes in spanwise direction	Δ	=	change in a parameter
Ma	=	Mach number	κ	=	permeability [m²]
n	=	number of holes in chordwise direction	ν	=	kinematic viscosity [m²/s]
p	=	local static pressure [N/m²]	ϕ	=	porosity
p_∞	=	freestream static pressure [N/m²]	ρ	=	density [kg/m³]
q	=	dynamic pressure [N/m²]			

II. Introduction

With the increased use of unmanned air vehicles in both civilian and military applications as well as small-scale turbines and high-altitude vehicles, there has been increasing interest in airfoils at Re between 10^4 and 10^5 [1–3]. This moderate Re regime is strongly influenced by laminar separation and by the possible formation of Laminar Separation Bubbles (LSB) where the separated shear layer transitions and reattaches, in the mean, as a turbulent boundary layer[4]. The presence of LSB's modifies the streamlines outside of the boundary layer, altering the effective shape of the airfoil. LSB's may also lead to hysteresis loops in the $C_\ell(\alpha)$ curve because the process for re-separation from the turbulent

---

*Graduate Student, Department of Aerospace and Mechanical Engineering, AIAA Student Member
†Professor, Department of Aerospace and Mechanical Engineering, AIAA Member

boundary layer state is not the same as the original transition. Careful examination of published lift-drag polars for moderate Re airfoils show a large fraction with multi-valued, non-monotonic profiles[5–8]. The laminar separation itself can lead to unusual phenomena. For example, the NACA 0012 at Re= 5×10^4 produces negative lift at small, positive α, followed by a lift slope, $C_{\ell_\alpha} > 2\pi$[9].

Birds and bats occupy a similar Re regime as many practical small-scale flying devices, so shapes and structures in the natural world may point to viable designs. The comparatively rough wings of swifts, for example, have been shown to reduce flow separation at Re<3.6×10^4[10, 11] as early promotion of turbulent transition is advantageous. It has also been observed that bird wing feathers have a large variation of permeability depending upon the feather type and location on the wing[12]. Force measurements made on the foremost primary feather of the White Stork (*Ciconia ciconia*) with and without an air seal showed an increase in L/D when air could pass through the feather[13]. The difference was mostly attributed to a reduction in drag, though the mechanism remained unclear.

Permeable wings at transonic Ma have successfully reduced wave drag by removing or diminishing the strength of shockwaves[14–16]. At speeds at which a shockwave would not form, drag was greatly increased. Reductions in drag and delay in separation are achievable by boundary layer suction through a porous wing surface, but the weight penalty and power required halted the further development of this technology for aircraft use. Thin airfoil theory and wind tunnel experiments suggest that permeability over large portions of the wing decreases L and C_{ℓ_α} and increases D [17–19]. Though cruise performance is reduced, permeable wings may still be of interest as a possible passive gust alleviation mechanism[17, 20].

This paper tests the idea that wing porosity could be advantageous for wing performance in this sensitive flow regime. When small holes allow communication between pressure and suction surfaces, the disturbance flows may be sufficient to change the flow state. This will be tested through direct force measurements and corroborated with dye visualization.

III. Materials and Methods

A. Wind Tunnel Tests

The Dryden Wind Tunnel at USC is a low-speed recirculating tunnel. The octagonal test section is 1.37 m wide with a turbulence level <0.035% for frequencies between 10 and 1000 Hz and mean speeds between 4 and 20 m/s. The excellent flow quality is attributed to the long and gradual 8:1 contraction ratio converging section downstream of 11 anti-turbulence screens. With flow speed set at a constant U=5 m/s, a chord-based Reynolds number was Re= $Uc/\nu = 5 \times 10^4$. Based on projected areas, the model and supports projected a 3.4% blockage at highest α; therefore, blockage effects were considered relatively small and neglected. Fig. 1 shows the model and test section configuration.
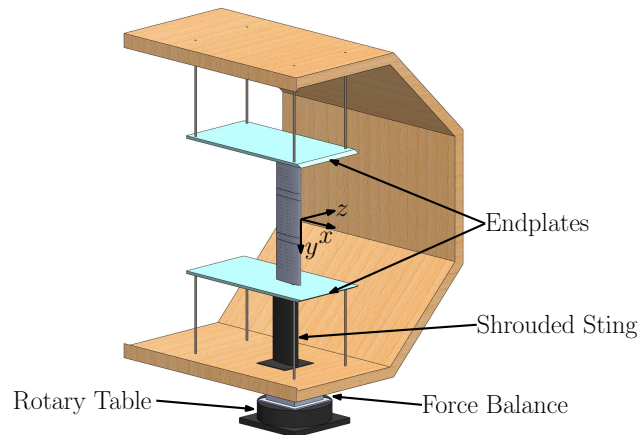

Fig. 1   Dryden Wind Tunnel test section with experimental setup.

Two rectangular NACA 0012 profile wings of c=15 cm, and b=60 cm, were 3D printed from PLA. The solid wing was printed in three sections on a MakerBot Replicator 2 with layer and x-y positioning resolution of 100 µm and 11 µm respectively. For the porous model, a Prusa i3 MK2 printer was used, with 50 µm layer resolution and 10 µm x-y position resolution. Due to build volume constraints, the porous model was printed in 5 sections. Seams for both

models were sealed with 1.3 cm wide, 0.20 mm thick, (1.1%t), duct tape. Measurements made using an Ambios XP-2 profilometer showed both printed models had comparable surface roughness. A 0.8 cm steel rod was inserted in the models at $c/4$ to be used for mounting in the wind tunnel

The porous model was printed with 1 mm, 0.67%c, holes oriented perpendicular to the chord line. The holes were arranged in a rectangular pattern starting at 10%c from the leading edge and spaced 10%c apart along the chord line. Holes were placed starting at 10%b and evenly spaced by 10%c in the spanwise direction, as shown in Fig. 2. In total, the porous wing had 297 holes. Estimating porosity, ϕ, as the ratio of the area of the holes, S_H, to the total planform area, S, $\phi = 0.003$.

To create a quasi-2D flow, endplates were mounted on either side of the model. The endplates had dimensions of 4.74c in x by 2.37c in z and a thickness of 0.08c. The laminar boundary layer thickness is $\delta = 4.91x/Re_x^{1/2} = 3.6$ mm at the leading edge of the model, where x is the distance from the leading edge of the endplate. The gap between the model and the endplate was less than 1 mm, or 0.27δ. A slot in the lower endplate at 1.44c from the plate leading edge and centered in the z direction allowed for the mounting rod to pass through.
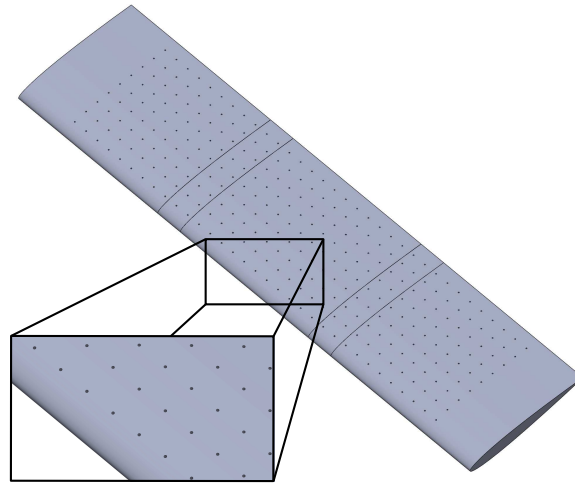
Fig. 2   CAD model of porous wing with zoomed image of the leading edge.

B. Force Balance Calibration and Measurements

A shrouded sting rested upon a custom, three-component, cruciform shaped force balance[21]. The balance was mounted to a rotary table, which set α, angle of attack. Axial and normal arms were calibrated by statically applying a range of expected loads. A calibration was completed before each test producing a 3-by-4 calibration matrix. To reduce random error from the calibration process, this matrix was then averaged with 2 previous matrices. This averaged matrix was used for experimental data collection. The measurement uncertainty of the balance in axial and normal directions were less than 5 mN and 15 mN, respectively.

Before each test, zeroing forces were recorded corresponding to the weight of the model. Each experiment consisted of 5 forward and backward α sweeps between -5° and 12° in 0.5° increments. After α was changed, the flow was allowed to settle for 10 s. Data was sampled at 1kHz for 10 s and averaged producing a single measurement. 10 measurements were then averaged yielding a single data point for each α. The standard deviation of these measurements was considered the uncertainty of this data point. Once these measurements were completed, a finer sweep in 0.1° increments was conducted at small α. The same procedure for each data point was used as above. The lift, L', and drag, D', per unit span are nondimensionalized by the dynamic pressure, q,

$$q = \frac{1}{2}\rho U^2 \tag{1}$$

and the chord length, c, yielding,

$$C_\ell = \frac{L'}{qc} \tag{2}$$

3

and,

$$C_{\mathrm{d}} = \frac{D'}{qc} . \tag{3}$$

C. Water Channel Experiments

The water channel at USC has a rectangular test section of height 61 cm and width of 89 cm. With a maximum achievable flow speed of 70 cm/s, the channel still maintains turbulence levels of <1%. Experiments were conducted at a water height of 48 cm. To maintain the same Re as wind tunnel experiments, the channel was run at U=16.7 cm/s, following sizing constraints described below.

Two arcylic wings were made with $b = 45$ cm and $c = 30$ cm. A rectangular hole pattern spaced at $0.1c$ was machined into one model. Hole diameter was 2 mm, the same chord fraction as the wind tunnel model.

As seen in Fig. 3, a flat plate of dimension $2.54c$ in x and $2.96c$ in z with $0.04c$ thickness was mounted above the wing to create quasi-2D flow as well as remove any free-surface effects. A hole was drilled in the center of the plate to allow for the wing mounting hardware. The bottom of the wing was flush with the bottom of the channel. To set α, a pin was used to align a rotor plate with a stator plate with known angles; α was also cross-checked from the images in postprocessing. α was varied from 0° to 2° with $\Delta\alpha = 0.5°$ and from 3° to 12° with $\Delta\alpha = 1.0°$. The stator plate was exchanged to acquire images between $\alpha = 0.2°$ and 1.2° with $\Delta\alpha = 0.2°$.
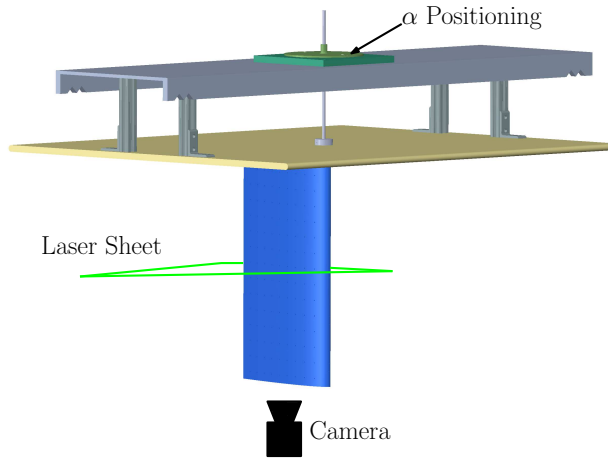
Fig. 3   Water channel experimental setup showing camera and laser sheet placement, as well as α positioning hardware.

Bright Dyes Fluorescent FWT Red 25 dye was diluted with water by a ratio of 40:1. The dye was injected from the leading edge at center span. A 5.14 W, 532 nm wavelength CNI wave laser was used to create a laser sheet that would illuminate the dye. Mounted below the channel, a Mako U-130 camera (1280×1024, 10 bit) with a Rainbow H6mm 1:1.2 lens was used to acquire flow visualization images. All images were post-processed to improve contrast, black levels, and invert colors.

IV. Results and Discussion

A. Force Balance Lift and Drag Measurements

Time-averaged lift and drag profiles for the NACA 0012 at Re = 5×10^4 are given in Fig. 4- 7, which also show previous reference data from the same profile shape in the same tunnel[9], which first established the phenomenon of negative lift at positive α. The observation of the 'N'-shaped curve around $\alpha = 0$ requires a very smooth geometry and quiet flow conditions, and is very sensitive to small disturbances. The $C_\ell(\alpha)$ is qualitatively similar but with local peak amplitudes in C_ℓ of about one half the reference values at $\alpha \pm 0.5$. Differences in surface roughness between the machined wing of Ref. [9] and the 3D printed article here likely account for the differences in C_ℓ, both at small α and for $\alpha > 4$. The important point is that all curves 4a- 5b are qualitatively similar, with previously remarked characteristic

features of sensitive dependence on the appearance and fore- or aft-motion of laminar separation bubbles. Finally the wing aspect ratio, $b/c = AR = 4$, and in Ref. [9], $AR = 6.5$ so end effects will be more influential here.
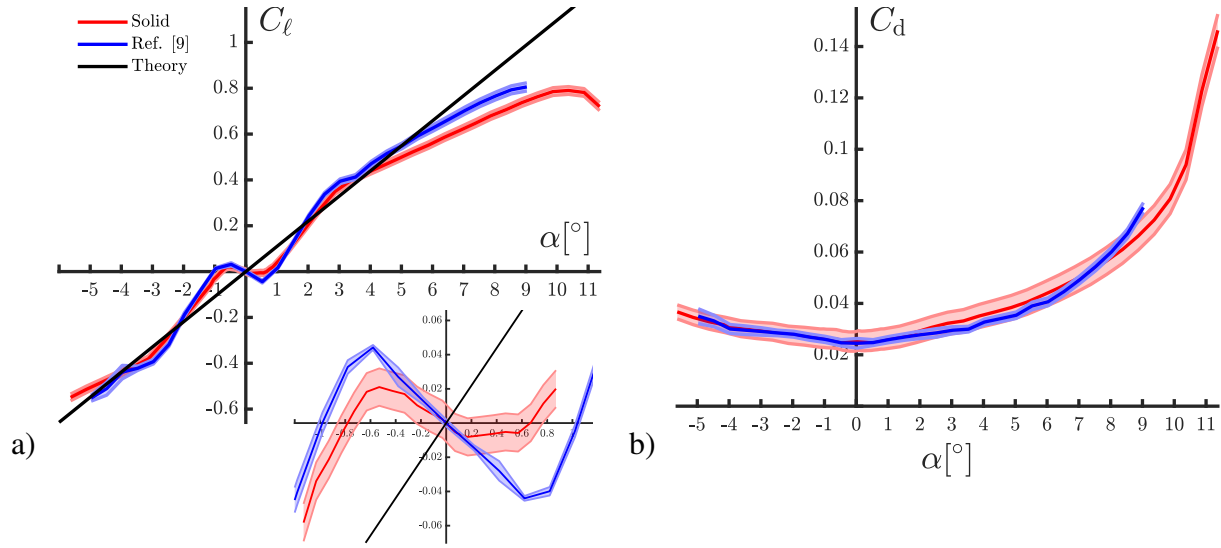

Fig. 4 **a** C_ℓ **and b** C_d **with uncertainty envelopes for a quasi-2D NACA 0012 at Re= 5×10^4 for the solid airfoil (red) with comparison to Ref.[9] (blue).**
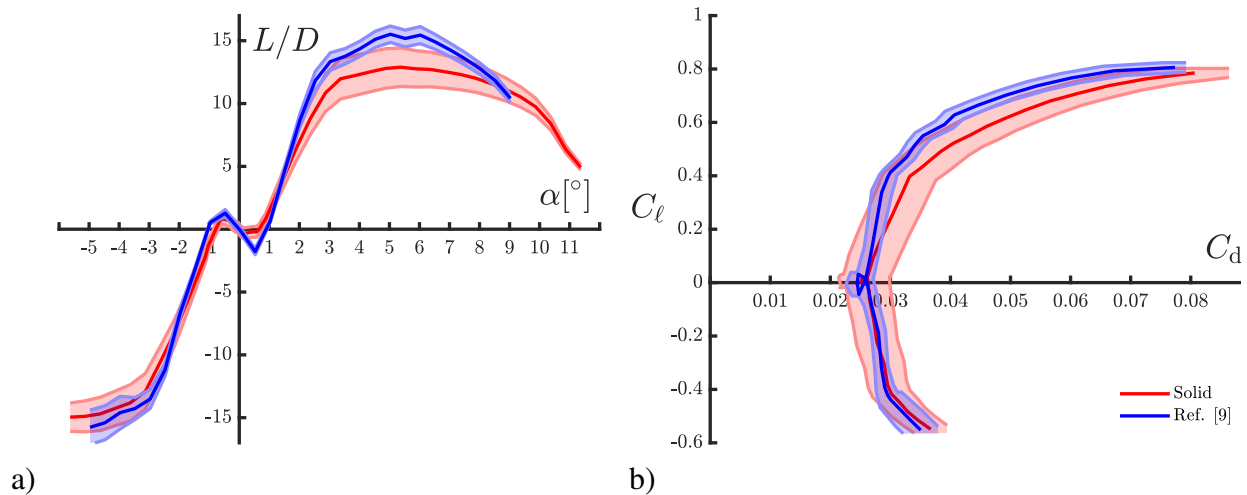

Fig. 5 **a** L/D **versus** α **and b drag polar for comparison between the solid airfoil (red) and Ref. [9] (blue).**

While making careful comparison with the reference case, there was no attempt to make a specially smooth finish on the 3D printed wing because the main comparison is not with Ref. [9], but will be with a similar wing with porous features. This comparison is given in Fig. 6 and Fig. 7.

Fig. 6a shows that the presence of holes in the porous wing almost completely straightens out the $C_\ell(\alpha)$ curve around $\alpha = 0$, removing the characteristic local positive and negative lift peaks. At the same time, there is no difference in C_d (Fig. 6b). There is a small decrease in C_ℓ at higher α but overall, within measurement uncertainty, L/D is equal to, or superior to the baseline wing at all α (Fig. 7). The porous wing always performs better than the solid one.

5
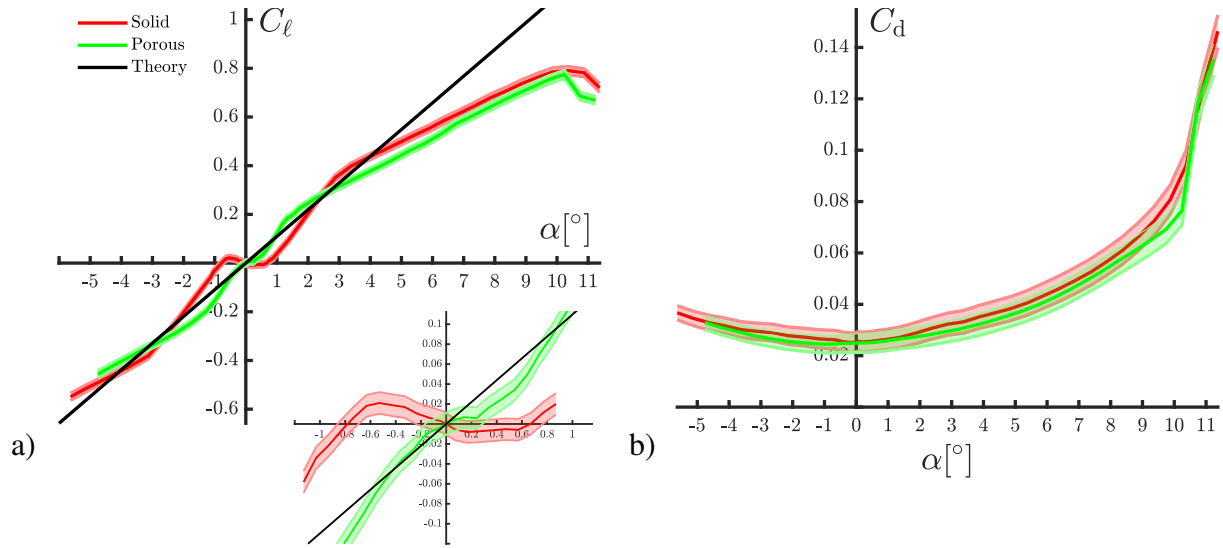
Fig. 6   a C_ℓ **and b** C_d **versus** α **of a solid (red) and porous (green) quasi-2D NACA 0012 wing at** $= 5 \times 10^4$**.**
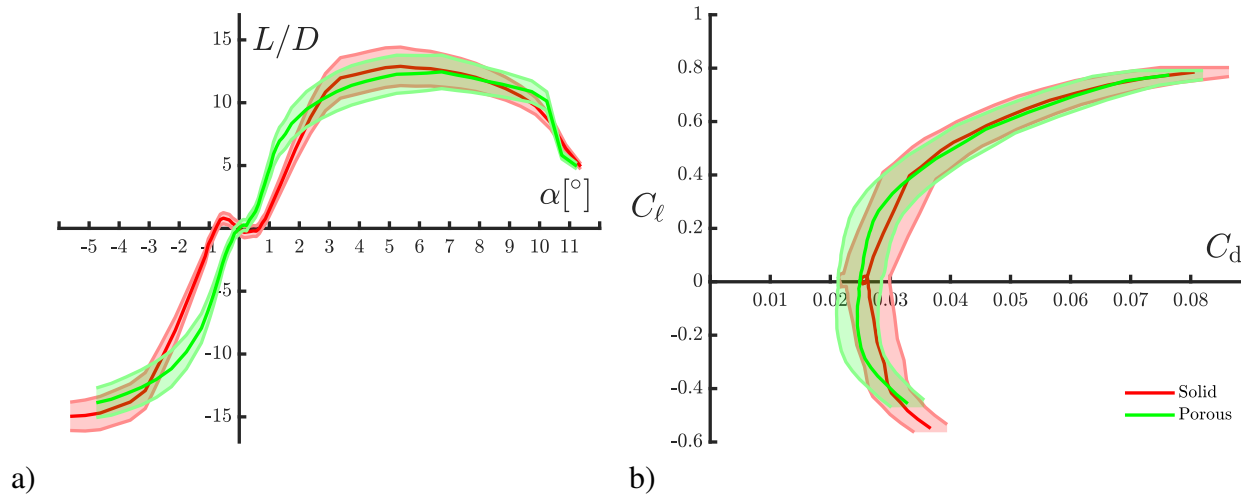

Fig. 7   a L/D **versus** α **and b drag polar for solid (red) and porous (green) wings.**

B. Dye Traces

When $\alpha = 0.0°$, von Kármán vortex streets are observed in the wake of both airfoils, shown in Fig. 8. Similar structures are observed at $\alpha = 0.2°$, commensurate with the similar values of C_ℓ at small α. The fluid close to the trailing edge of the porous airfoil at $\alpha = 0.4°$ begins to form small eddies, slightly disrupting the main wake eddies. Meanwhile, the flow about the solid wing shows no equivalent destabilizing disturbances on the von Kármán vortex street. As α increases, the regular alternating wake feature is more clearly contaminated with smaller scale features and at $\alpha = 0.8°$ the amplitude of the vortex street deflections is much reduced compared with the solid wing counterpart. The small-scale eddies that eventually disrupt the Kármán street seem to originate in the boundary layer on both upper and lower wing surfaces.

Pixel values were averaged over 1,300 images for each α producing images such as Fig. 9. The streamwise separation location, $\overline{x}_s$, defined as the chord location of separation normalized by c, was estimated from the time-averaged images for each α and plotted in Fig. 10. Between $1° \leq \alpha < 7°$, $\overline{x}_s$ of the porous airfoil is further downstream than that of the solid airfoil for a given α. The range of higher $\overline{x}_s$ coincides very closely with the range of measurably-different $C_\ell(\alpha)$ between the solid and porous wings (see Fig. 6a). C_ℓ may be lower ($\alpha \leq 2$), or higher ($2 < \alpha \leq 7$). The most practical consequence is that the lift slope, C_{ℓ_α}, is much more uniform over the entire range. Close to $\alpha = 0°$, the separation

6
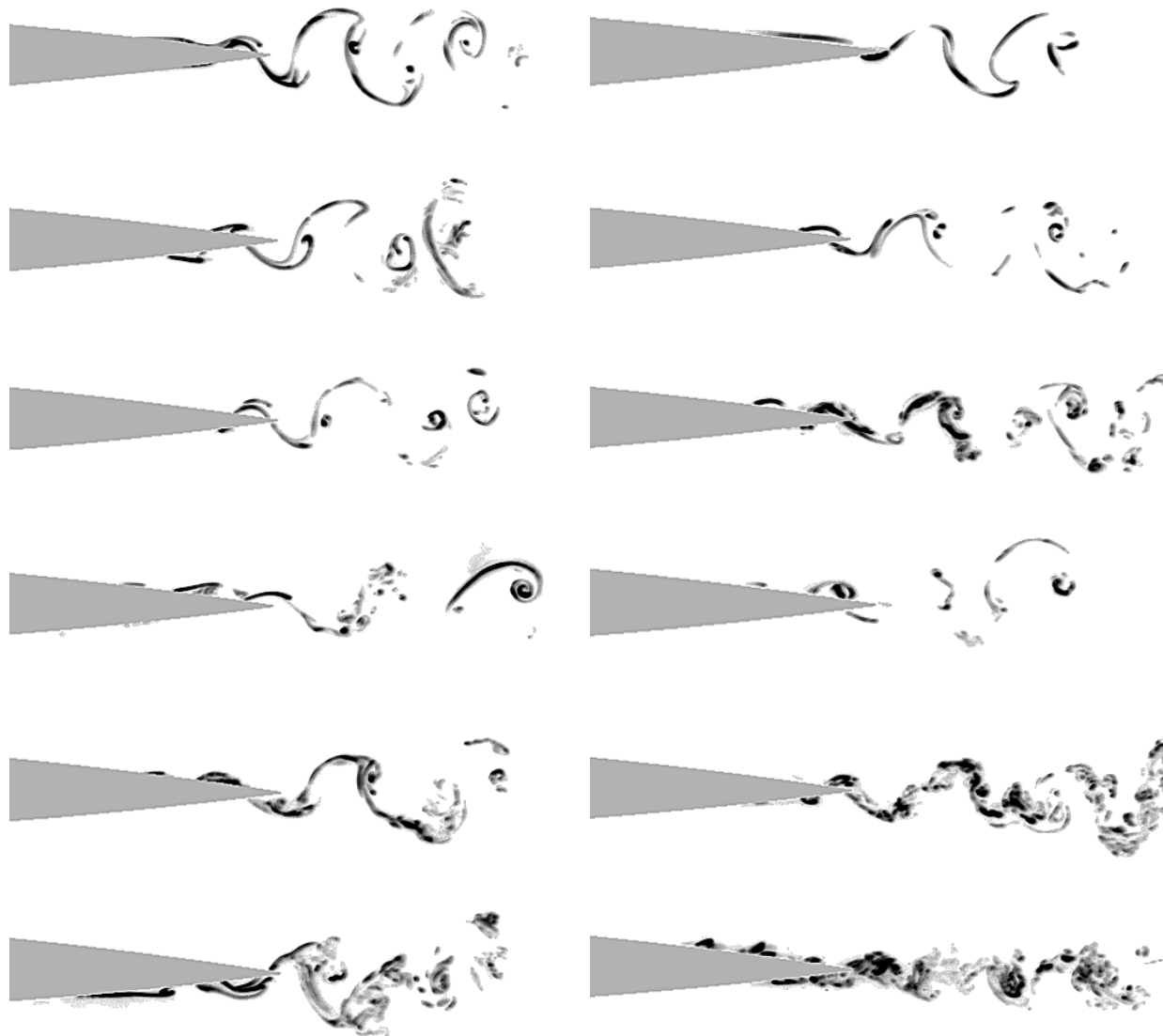
Fig. 8 Instantaneous dye images for $\alpha = [0.0, 0.2, 0.5, 0.4, 0.8^\circ]$**. Images on the left are of the solid airfoil; those on the right are of the porous airfoil.**

locations are quite similar and both have a sharp notch, corresponding to a more forward location, at $\alpha = 0.5^\circ$. The notch is due to a small re-circulation region that is established near the trailing edge of both solid and porous wings at this α. There is no special feature of the $C_\ell(\alpha)$ curves at this α. The airfoil-driven pressure difference itself drives a flow disturbance that leads to small-scale features that promote later boundary-layer separation. Though the force measurements and time-averaged dye images that lead to mean separation location measurements lend themselves to time-averaged interpretation, the flow towards the trailing edge, and so the pressure difference that causes the small perturbations, are never steady.

The small eddies formed in the boundary layer and wake of the porous airfoil, shown in Fig. 8, will lead to small perturbations to the fluid flow. These perturbations, somehow, lead to the straightening of the lift curve seen in Fig. 6a near $\alpha = 0.0^\circ$. As shown in Fig. 11, the pressure difference between the suction and pressure surfaces may be imagined to induce a (fluctuating) fluid flow through the wing, causing a local disturbance to the boundary layer at the pore.

Some quick estimates of the magnitude of the pressure disturbance and subsequent wall-normal flow may be made, and XFOIL[22], a panel code, was used to compute the pressure distributions on a solid NACA 0012 at Re= 5×10^4.

7
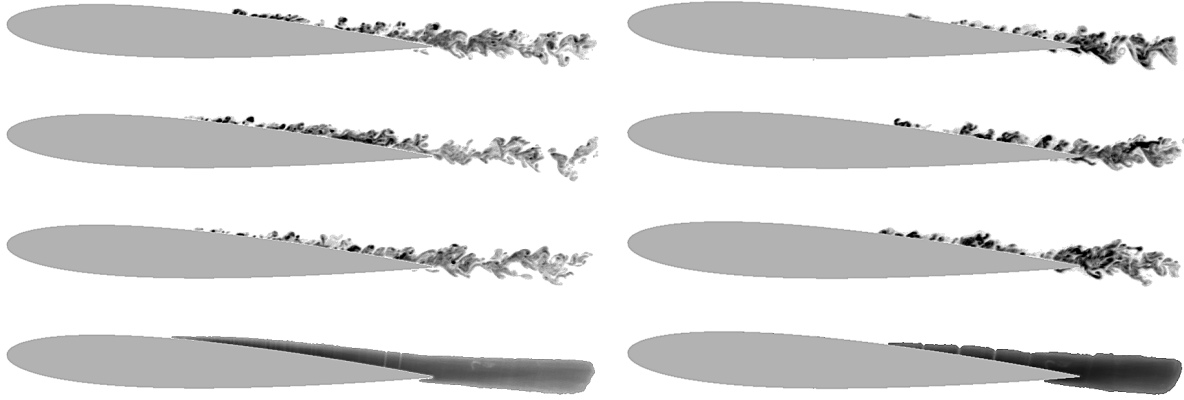
Fig. 9   Three instantaneous flow fields at $\alpha = 3.0°$. Below, is the time-averaged image of 1,300 frames. Solid on left; porous on right.
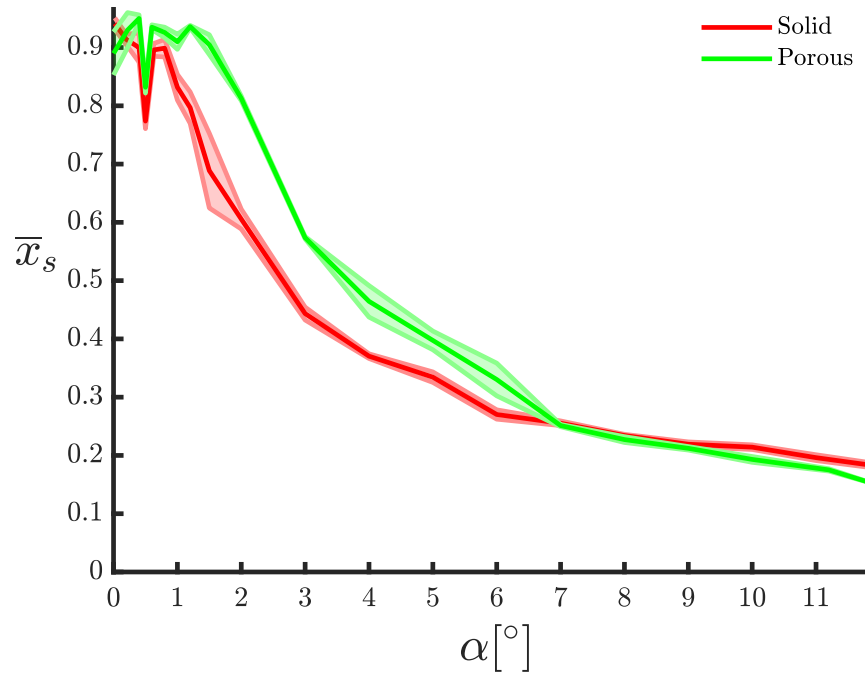

Fig. 10   Streamwise separation location, estimated from time-averaged dye images for the solid and porous NACA 0012 at Re= 5×10^4.

The pressure coefficient, C_p, is defined as,

$$C_p = \frac{p - p_\infty}{q} , \tag{4}$$

where p and p_∞ are the local and freestream static pressures, respectively. The change of C_p between both surfaces at the chordwise locations of the pores, ΔC_p, was estimated. Then, the flow through a given pore may be approximated by the Darcy-Weisbach equation,

$$\Delta p = f \frac{l_i}{d} \frac{\rho u_\perp^2}{2} , \tag{5}$$

8
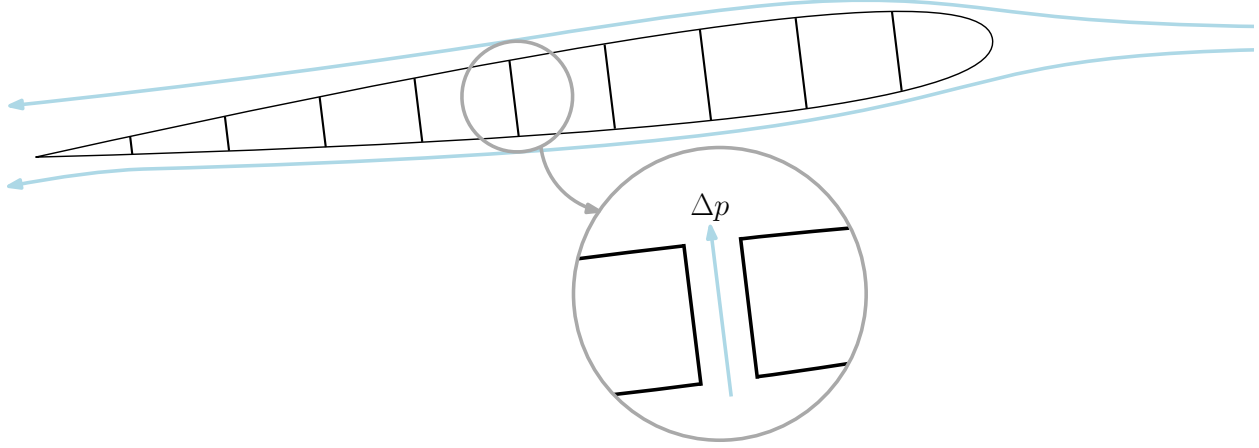
Fig. 11   Mechanism of pressure driven porous airfoil flow.

where l_i and d are the length and diameter of the pore, respectively. It is assumed the pore is sufficiently small, such that Δp does not vary over the face of the pore. The friction factor, f, is defined as,

$$f = \frac{64}{\mathrm{Re}_d} \,, \tag{6}$$

and

$$\mathrm{Re}_d = \frac{u_\perp d}{\nu} \,. \tag{7}$$

Combining and rearranging Eqs. (5-7) produces,

$$u_\perp = \frac{d^2}{32\nu l_i \rho} \Delta p \,. \tag{8}$$

Nondimensionalizing Eq. (8) by U, q, and c produces,

$$\frac{u_\perp}{U} = \frac{(d/c)^2}{64(l_i/c)} \mathrm{Re}\Delta C_{\mathrm{p}} \,. \tag{9}$$

Note, l_i/c is a function of the chordwise location of the pore, and d/c is a constant. Seen in Fig. 12, the pores aft of midchord exhibit a more negative $\overline{u}_\perp$ at low α than pores closer to the leading edge. The suction at the pore will perturb the boundary layer normal to the wall. These perturbations lead to the global lift changes observed in Fig. 6a.

For a permeable medium, the volume flow rate due to a pressure difference is determined by Darcy's law, or,

$$Q = \frac{\kappa S}{\rho \nu t} \Delta p \,, \tag{10}$$

where κ, a dimensional parameter, is the permeability. Q can also be estimated for a porous wing by multiplying Eqn. (8) by the pore area and summing over all pores yielding,

$$Q = m \frac{\pi d^4}{128\nu\rho} \Delta p \sum_{i=1}^{n} \frac{1}{l_i} \,. \tag{11}$$

m and n are the number of holes in the spanwise and streamwise directions, respectively. Combining Eqns. (11) and (10) and simplifying produces,

$$\kappa = \frac{d^2 t}{32n} \phi \sum_{i=1}^{n} \frac{1}{l_i} \,. \tag{12}$$

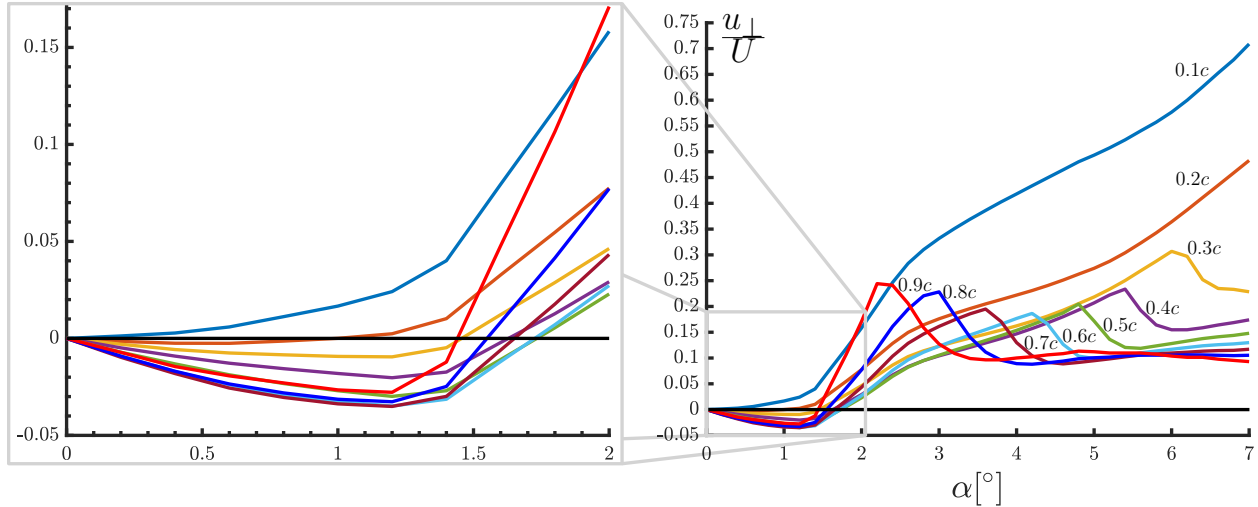Assuming $l_i \approx t$, simplifies Eqn. (12) further to,

9

Fig. 12 $u_\perp/U$ **computed using Eqn. 9 and XFOIL** C_p **results at Re**$= 5 \times 10^4$**.**

$$\kappa = \frac{d^2}{32}\phi \ . \tag{13}$$

κ is estimated to be 80 μm^2 and 390 μm^2 for the wind tunnel and water channel models, respectively. Because κ is a dimensional quantity, it should vary with geometry changes despite Re being held constant. $\overline{u}_\perp$, however, is consistent between both wind tunnel and water channel experiments meaning the flow physics are similar. Low values of κ are to be expected because the majority of the airfoil is solid, yet this still has a significant effect on the airfoil performance.

V. Conclusion

This study examined a quasi-2D NACA 0012 at Re$= 5 \times 10^4$ with both solid and porous surfaces. Wind tunnel experiments measured $C_\ell(\alpha)$ and $C_d(\alpha)$. The solid airfoil showed qualitative agreement with a previous, comparable study. At small, positive α, negative lift is produced, a counterintuitive result. When low porosity between the pressure and suction surfaces is introduced, the anomalous behavior is removed without a measurable drag or L/D penalty. Dye visualization combined with XFOIL analysis show that porosity can allow a flow through the airfoil to perturb the boundary layer, sufficient to cause significant changes in the lift profile. The intrinsic flow sensitivity can lead to amplification of disturbances, which may be used deliberately for effective control, either passive or active.

Acknowledgments

References

[1] Laitone, E., "Wind tunnel tests of wings at Reynolds numbers below 70 000," *Experiments in Fluids*, Vol. 23, No. 5, 1997, pp. 405–409. doi:10.1007/s003480050128.

[2] Mueller, T. J., and Batil, S. M., "Experimental studies of separation on a two-dimensional airfoil at low Reynolds numbers," *AIAA journal*, Vol. 20, No. 4, 1982, pp. 457–463. doi:10.2514/3.51095.

[3] Yarusevych, S., Sullivan, P. E., and Kawall, J. G., "On vortex shedding from an airfoil in low-Reynolds-number flows," *Journal of Fluid Mechanics*, Vol. 632, 2009, pp. 245–271. doi:10.1017/s0022112009007058.

[4] Mueller, T. J., "The influence of laminar separation and transition on low Reynolds number airfoil hysteresis," *Journal of Aircraft*, Vol. 22, No. 9, 1985, pp. 763–770. doi:10.2514/3.45199.

10

[5] Simons, M., and Simons, M., *Model aircraft aerodynamics*, Nexus Special Interests Hemel Hempstead, UK, 1999.

[6] Selig, M. S., Guglielmo, J. J., Broeren, A. P., and Giguére, P., *Summary of Low-Speed airfoil data*, Vol. 1, SoarTech, 1995.

[7] Selig, M. S., Lyon, C. A., Giguére, P., Ninham, C. P., and Guglielmo, J. J., *Summary of Low-Speed airfoil data*, Vol. 2, SoarTech, 1996.

[8] Lyon, C. A., Broeren, A. P., Giguére, P., Gopalarathnam, A., and Selig, M. S., *Summary of Low-Speed airfoil data*, Vol. 3, SoarTech, 1997.

[9] Tank, J., Smith, L., and Spedding, G., "On the possibility (or lack thereof) of agreement between experiment and computation of flows over wings at moderate Reynolds number," *Interface focus*, Vol. 7, No. 1, 2017, p. 20160076. doi:10.1098/rsfs.2016.0076.

[10] Lentink, D., and de Kat, R., "Gliding Swifts Attain Laminar Flow over Rough Wings," *PLOS ONE*, Vol. 9, No. 6, 2014, pp. 1–8. doi:10.1371/journal.pone.0099901, URL https://doi.org/10.1371/journal.pone.0099901.

[11] van Bokhorst, E., de Kat, R., Elsinga, G. E., and Lentink, D., "Feather roughness reduces flow separation during low Reynolds number glides of swifts," *Journal of Experimental Biology*, Vol. 218, No. 20, 2015, pp. 3179–3191. doi:10.1242/jeb.121426, URL http://jeb.biologists.org/content/218/20/3179.

[12] Müller, W., and Patone, G., "Air Transmissivity of Feathers," *Journal of Experimental Biology*, Vol. 201, 1998, pp. 2591–2599.

[13] Eder, H., Fiedler, W., and Pascoe, X., "Air-Permeable Hole-Pattern and Nose-Droop Control Improve Aerodynamic Performance of Primary Feathers," *J. Comp. Physiol. A*, Vol. 197, 2011, pp. 109–117. doi:10.1007/s00359-010-0592-7.

[14] Savu, G., and Trifu, O., "Porous Airfoils in Transonic Flow," *AIAA Journal*, Vol. 22, 1984, pp. 989–991. doi:10.2514/3.48535.

[15] Nagamatsu, H. T., Orozco, R. D., and Ling, D. C., "Porosity Effect on Supercritical Airfoil Drag Reduction by Shock Wave/Boundary Layer Control," *AIAA 17th Fluid Dynamics, Plasma Dynamics, and Lasers Conference*, AIAA, Snowmass, CO, 1984.

[16] Hartwich, P. M., "Euler study on porous transonic airfoils with a view toward multipoint design," *Journal of Aircraft*, Vol. 30, 1993, pp. 184–191. doi:10.2514/3.48264.

[17] Iosilevskii, G., "Aerodynamics of Permeable Membrane Wings," *European Journal of Mechanics-B/Fluids*, Vol. 30, 2011, pp. 534–542. doi:10.1016/j.euromechflu.2011.05.003.

[18] Iosilevskii, G., "Aerodynamics of Permeable Membrane Wings. Part 2: Seepage drag," *European Journal of Mechanics-B/Fluids*, Vol. 39, 2013, pp. 32–41. doi:10.1016/j.euromechflu.2012.11.004.

[19] Geyer, T., and Sarradj, E., "Trailing Edge Noise of Partially Porous Airfoils," *20th AIAA/CEAS Aeroacoustics Conference*, AIAA, Atlanta, GA, 2014.

[20] Aldheeb, M., Asrar, W., Sulaeman, E., and Omar, A. A., "Aerodynamics of Porous Airfoils and Wings," *Acta Mechanica*, Vol. 229, No. 9, 2018, pp. 1–19. doi:10.1007/s00707-018-2203-6.

[21] Zabat, M., Frascaroli, S., Browand, F., Nestlerode, M., and Baez, J., "Drag Measurements on a Platoon of Vehicles," Tech. rep., 1994.

[22] Drela, M., "XFOIL: An analysis and design system for low Reynolds number airfoils," *Low Reynolds number aerodynamics*, Springer, 1989, pp. 1–12.